

See discussions, stats, and author profiles for this publication at: <https://www.researchgate.net/publication/231648986>

# Metal Oxide Catalysts for the Evolution of O<sub>2</sub> from H<sub>2</sub>O

ARTICLE *in* THE JOURNAL OF PHYSICAL CHEMISTRY C · FEBRUARY 2008

Impact Factor: 4.77 · DOI: 10.1021/jp710675m

---

CITATIONS

69

---

READS

40

2 AUTHORS, INCLUDING:



**Matthew Donovan Merrill**

Luna Innovations, Inc.

**19** PUBLICATIONS **844** CITATIONS

SEE PROFILE

# Metal Oxide Catalysts for the Evolution of O<sub>2</sub> from H<sub>2</sub>O

Matthew D. Merrill and Ralph C. Dougherty\*

Department of Chemistry and Biochemistry, Florida State University, Tallahassee, Florida 32306-4390

Received: November 7, 2007

This paper describes an iron-nickel oxide catalyst that can eliminate oxygen overvoltage in the electrolysis of alkaline water. Oxygen overvoltage is the largest source of energy loss in water electrolysis. A method for cathodic electrodeposition of first-row transition metal oxides for use as catalysts is described, and the effects of the electrodeposition variables on catalytic performance and catalyst composition were explored. The NiFe oxide catalyst achieved a nearly ideal anodic electron-transfer coefficient,  $\alpha_a = 0.0082$  (14.8 mV/decade) in a 1 M KOH solution. The metal oxide catalysts reported here could produce hydrogen and oxygen from water at approximately the thermodynamic potential for small currents. Both transmission electron microscopy and X-ray photoelectron spectroscopy experiments indicated that the NiFe oxide was composed of small crystals ( $\sim 1$  nm) connected with an amorphous phase and contained a highly disordered arrangement of all nonmetallic nickel and iron oxidation states. Changes in electrochemical impedance spectra (EIS) with applied working potential correlated with known nickel and iron aqueous reduction potentials. A simple catalytic mechanism is presented. EIS showed a high-frequency inductive loop that spanned 3 log of frequency ( $> 10^5$  to  $\sim 10^2$  Hz) and exhibited both negative capacitance and negative resistance. A scan of electrode material (scraped from the electrode) magnetization as a function of applied magnetic field using a SQUID magnetometer showed the NiFe oxide electrode to have magnetically ordered domains within its structure and to have a magnetization at zero-applied field. Magnetic fields associated with these domains are related to the efficient production of the oxygen triplet state with the electrode. These fields are also responsible for the fact that the oxygen-evolving electrode will not produce a cyclic voltammogram but rather gives an oscillating signal indicating charge rearrangement under those conditions.

## Introduction

The interconversion of water and oxygen gas is a fundamental chemical feature in biological and global energy systems. The biological evolution of water oxidation in photosynthesis transformed the earth's surface from anaerobic to aerobic roughly 3 billion years ago. The production of oxygen gas from water by photosynthesis allows the storage of energy in biological electron carriers such as NADPH, which can be considered a biological equivalent to H<sub>2</sub>. The adoption of an energy economy based on hydrogen fuel from water is biologically compatible as long as the energy source is renewable.

The energy required for production of hydrogen and oxygen from water can be obtained by on-site generation of electricity. Water electrolysis allows for the small/medium-scale production of hydrogen gas in a distributed energy system. Distributed energy systems avoid the cost and energy losses associated with transporting fuel from a centralized production facility.

The overvoltage of the oxygen evolution reaction has been the largest source of energy loss in water electrolysis. The major source of this overvoltage is the spin inversion required to produce triplet oxygen.<sup>1</sup> Our development of oxygen evolution catalysts began by assessing enzymes that catalyze oxygen evolution and oxygen reduction reactions. Photosystem II efficiently produces oxygen in the triplet-state with an overvoltage of  $\sim 0.1$  eV.<sup>2</sup> The overpotential for cytochrome C oxidase is less than 0.3 V for oxygen reduction.<sup>3</sup> The transition metal ions of the photosystem II (Mn) and cytochrome C oxidase

(Fe and Cu) catalytic sites bind oxygen and water ligands during the catalytic cycle. The conclusions developed from studying biological reactions were that the catalytic properties of transition metal oxides ranging from Mn to Cu should be carefully explored for the oxygen evolution reaction. Co and Ni oxides were included in the exploration of Mn, Fe, and Cu oxides because they share many of the same stable aqueous oxidation states with relatively similar reduction potentials. The scope of this work was confined to the first-row transition metals because these metals have smaller d orbitals compared to other metals and therefore have smaller crystal field activation energies for transitions between oxidation states.<sup>4</sup> The metals from Mn to Cu are also ideal because their natural abundance results in affordable and economical catalysts with minimum toxicity.

The catalysts presented here were produced through the cathodic electrodeposition of metal oxides onto a platinum support. Nickel oxide electrodes formed from cathodic electrodeposition have been available for over 100 years.<sup>5</sup> It has long been known that iron impurities in nickel oxide batteries facilitate the oxygen evolution reaction, which is parasitic to the battery charging process.<sup>6</sup> Dennis A. Corrigan redirected work originally focused on cathodically deposited nickel oxide battery applications toward iron-doped nickel oxide catalysts for alkaline water electrolysis in the 1980s.<sup>6–15</sup>

Advances in the cathodic electrodeposition technique reported here included use of electrolytes other than strong acids in the electrodeposition solution as well as the effects of higher power densities. Electrolytes such as ammonium salts and organic acids were included in the electrodeposition solution as mimics of catalytic site ligands observed in enzyme examples. Ligands of

\* To whom correspondence should be addressed. E-mail: ralphd@chem.fsu.edu.

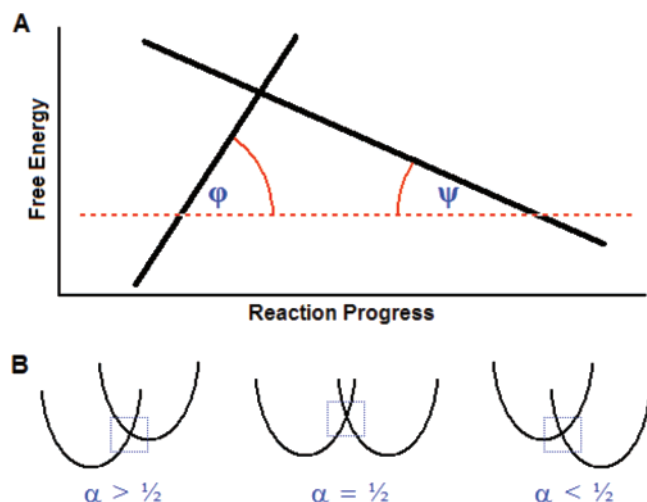


**Figure 1.** (A) The transfer coefficient,  $\alpha$ , of the Butler–Volmer model is determined by angles of the intersecting classical harmonic oscillators. (B) The  $\alpha$ -values for various scenarios where harmonic oscillators intersect (boxes) although the  $\alpha$ -value does not necessarily reflect reduction or oxidation reactions as illustrated.

these types are significantly nucleophilic toward transition metal ions and can be expected to significantly alter the electrode preparation chemistry. The use of high electrodeposition current densities was expected to increase electrocatalytic activity by promoting the presence of defects in the metal oxide matrix of the catalyst.<sup>16,17</sup> The catalytic properties of the metal oxides can be influenced through other variables of the electrodeposition reaction such as the total and relative concentration(s) and composition(s) of dissolved metal salts and extra electrolytes, the pH, and the duration of the electrodeposition current. The cathodic electrodeposition reaction was a simple method by which large numbers of catalyst compositions were explored quickly and efficiently.

Our assessment of catalyst performance was based on four catalyst kinetic parameters. Two kinetic parameters described how current was exponential with respect to working potential at low-current densities and two kinetic parameters described how current was linear with respect to working potential at high-current densities. Water electrolysis at high-current densities may be necessary for some practical applications. The catalytic kinetics at low currents are called Butler–Volmer kinetics and the kinetics at high currents are called resistive kinetics.

Butler–Volmer kinetics use eqs 1 and 2. These equations are used for the oxygen evolution and hydrogen evolution reactions, respectively. Our Butler–Volmer models assume a negligible reverse current, where  $J$  is current density,  $J_0$  is exchange current density,  $\alpha$  is the electron-transfer coefficient,  $n$  is the number of  $e^-$  per reaction,  $F$  is Faraday's constant,  $R$  is ideal gas law constant,  $T$  is absolute temperature,  $E$  is working potential, and  $E_0$  is the calculated equilibrium potential. The  $\alpha$  and  $J_0$  values are the two Butler–Volmer kinetic performance parameters and were determined through linear regression of a Tafel plot (see Figure 3) where the kinetics demonstrated a linear free energy relationship. The  $J_0$  pre-exponential factor should have the highest value possible for optimum kinetic performance.

$$J = J_0 \times \exp\left[\frac{(1 - \alpha_a)nF(E - E_0)}{RT}\right] \quad (1)$$

$$J = J_0 \times \exp\left[\frac{(\alpha_c)nF(E - E_0)}{RT}\right] \quad (2)$$

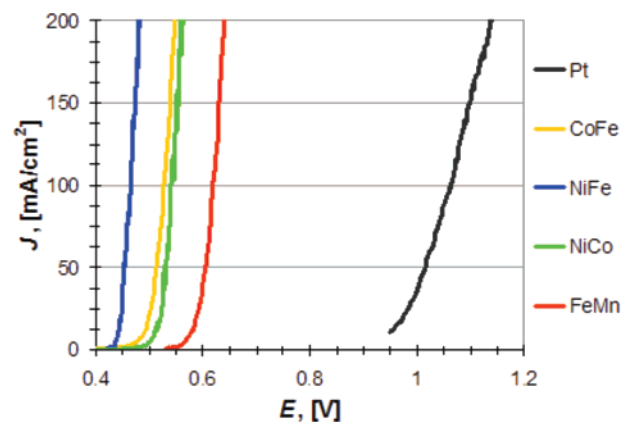


**Figure 2.** Linear voltammetry scans at a rate of 1 mV/s for selected metal oxide compositions and the platinum support in 1 M KOH.

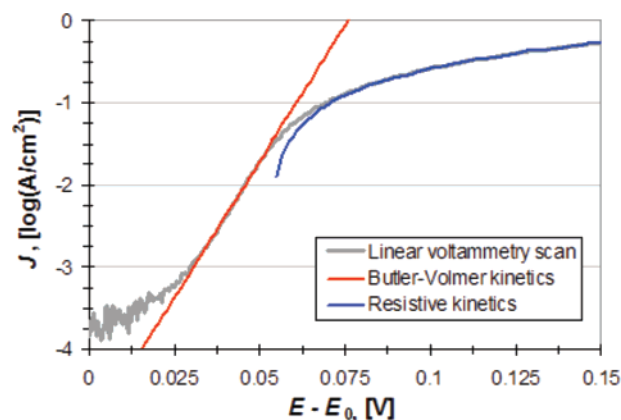


**Figure 3.** An oxygen evolution Tafel plot for a NiFe<sub>(a)</sub> oxide catalyst, and the kinetic data was collected with a linear voltammetry scan at a scan rate of 1 mV/s in 1 M KOH, where  $E_0$  was 0.399 V.

The transfer coefficient,  $\alpha$ , of the Butler–Volmer model classically describes the symmetry of the electron-transfer energy barrier. The  $\alpha$  value represents the symmetry of interacting harmonic oscillators according to eq 3 where  $\phi$  and  $\psi$  refer to the angles illustrated in Figure 1A. The angles of Figure 1A represent the angles of the intersecting harmonic oscillators illustrated in the boxes of Figure 1B. The angles of the intersections themselves do not necessarily indicate whether transfer is to higher or lower energy oscillators as represented in Figure 1B. The ideal  $\alpha$ -value for the anodic oxygen evolution reaction is 0, and the ideal  $\alpha$ -value for the cathodic hydrogen evolution reaction is 1. An ideal  $\alpha$ -value represents the angles at which  $\phi$  and  $\psi$  produce the smallest energy barrier possible. Anodic and cathodic electron-transfer coefficients are designated as  $\alpha_a$  and as  $\alpha_c$ , respectively.

$$\alpha = \frac{\tan(\phi)}{\tan(\phi) + \tan(\psi)} \quad (3)$$

The catalytic kinetics at high-current densities was referred to as resistive because current was linear with respect to voltage. The Butler–Volmer model as described by eqs 1 and 2 did not adequately describe the catalytic kinetics at high-current densities. Equation 4 is a form of Ohm's law used for describing high-current kinetics where  $J$  is current density,  $E$  is working potential,  $E_0$  is the calculated equilibrium potential,  $R_{lim}$  is the limiting resistance area, and  $J_b$  is the  $Y$ -intercept current density value. The  $R_{lim}$  and  $J_b$  values are the two resistive performance parameters and were determined by linear regression where the relationship of current density with respect to working potential

**TABLE 1: Electrodeposition Solution Conditions<sup>a</sup>**

oxide	metal salt(s)	electrolyte(s)	pH
Mn	18 mM MnSO <sub>4</sub>	125 mM NH <sub>4</sub> ClO <sub>4</sub>	1.5 w/ H <sub>2</sub> SO <sub>4</sub>
Fe	18 mM FeSO <sub>4</sub>	100 mM NH <sub>4</sub> ClO <sub>4</sub>	1.5w/ H <sub>2</sub> SO <sub>4</sub>
Co	18 mM CoSO <sub>4</sub>	35 mM NH <sub>4</sub> ClO <sub>4</sub>	6.8 w/ NH <sub>4</sub> OH
Ni	18 mM NiSO <sub>4</sub>	25 mM NH <sub>4</sub> ClO <sub>4</sub>	6.0 w/ NH <sub>4</sub> OH
Cu	10 mM CuSO <sub>4</sub>	30 mM NH <sub>4</sub> ClO <sub>4</sub>	5.0 w/ NH <sub>4</sub> OH
FeMn	9 mM FeSO <sub>4</sub> and 9 mM MnSO <sub>4</sub>	87.5 mM NH <sub>4</sub> ClO <sub>4</sub>	2.5 w/ H <sub>2</sub> SO <sub>4</sub>
CoFe	10 mM CoSO <sub>4</sub> and 9 mM FeSO <sub>4</sub>	30 mM NH <sub>4</sub> ClO <sub>4</sub>	5.4 w/ NH <sub>4</sub> OH
NiFe <sub>(a)</sub>	9 mM NiSO <sub>4</sub> and 9 mM FeSO <sub>4</sub>	25 mM (NH <sub>4</sub> ) <sub>2</sub> SO <sub>4</sub>	2.5 w/ NH <sub>4</sub> OH
NiFe <sub>(b)</sub>	9 mM NiSO <sub>4</sub> and 9 mM FeSO <sub>4</sub>	25 mM (NH <sub>4</sub> ) <sub>2</sub> SO <sub>4</sub>	5.9 w/ NH <sub>4</sub> OH
NiCo	9 mM NiSO <sub>4</sub> and 9 mM CoSO <sub>4</sub>	25 mM NH <sub>4</sub> ClO <sub>4</sub>	6.6 w/ NH <sub>4</sub> OH
CuFe	9 mM CuSO <sub>4</sub> and 9 mM FeSO <sub>4</sub>	50 mM NH <sub>4</sub> ClO <sub>4</sub>	4.2 w/ H <sub>2</sub> SO <sub>4</sub>
CuNi	9 mM CuSO <sub>4</sub> and 9 mM NiSO <sub>4</sub>	30 mM NH <sub>4</sub> ClO <sub>4</sub>	7 w/ NH <sub>4</sub> OH

<sup>a</sup> The catalysts were deposited at 250 mA/cm<sup>2</sup> for 30 s.

was linear at high-current densities. For optimum catalyst performance,  $R_{\text{lim}}$  should be as small as possible and  $J_b$  should be as small as possible.

$$J = \frac{E - E_0}{R_{\text{lim}}} + J_b \quad (4)$$

## Experimental Section

The electrochemical experiments were conducted with a Radiometer Analytical Voltalab 10 (PGZ100) electrochemical workstation operated by VoltaMaster 4 software. The three-electrode electrochemical cell consisted of a working (1 cm<sup>2</sup>), a counter electrode (1 cm<sup>2</sup>), and an Accument saturated Ag/AgCl reference electrode (13-620-53). The tip of the reference electrode was placed in contact with the catalyst/electrolyte interface of the working electrode. The working and counter electrodes were square 1 cm × 1 cm × 25 μm platinum foil with Starbrite liquid electrical tape insulating the back side of the platinum and the 30 gage platinum connecting wire so that only one flat surface, 1 cm<sup>2</sup>, was exposed to the electrolyte. Larger samples of catalysts were deposited by an Agilent N2766A power source onto both sides of a 4 cm × 2.5 cm × 25 μm platinum foil with two parallel, equal sized counter electrodes placed 0.5 cm away on both sides. Platinum (Hauser and Miller) was selected for use as a control and a recyclable, conductive support for deposition of the catalysts. Fresh, concentrated sulfuric acid was used to dissolve the catalysts from the platinum after use and to polish the platinum immediately prior to use.

The oxygen evolution reaction was analyzed in 100 mL samples of KOH electrolyte open to the atmosphere (295–298 K). All solutions were prepared with water purified to 18 Mohm resistance (Barnstead, EASYPure UV). Ambient 1 M KOH is considered to have a pH of 13.84 as determined theoretically and experimentally by the ionic activity coefficients correlated with the Khoshkbarchi–Vera equation and new hydration theory.<sup>18</sup> Equation 5 is used to calculate the water oxidation equilibrium potential,  $E^0_{\text{O}_2}$ , of 0.399 V when considering an atmospheric O<sub>2</sub> partial pressure of 0.2095 atm.<sup>19,20</sup> Equation 6 is used to calculate the water reduction equilibrium potential,  $E^0_{\text{H}_2}$ , of −0.945 V when considering an atmospheric H<sub>2</sub> partial pressure of  $5 \times 10^{-5}$  atm.<sup>19,20</sup> The  $E^0_{\text{H}_2}$  is offset 1.481 V from  $E^0_{\text{O}_2}$  in alkaline conditions because the thermodynamic requirement for water electrolysis is considered to be the  $\Delta H$  of water formation.<sup>21,22</sup>

$$E^0_{\text{O}_2} = 1.228 \text{ V} - 0.05916(\text{pH}) + 0.0147[\log(\text{pO}_2)] = 0.399 \text{ V} \quad (5)$$

$$E^0_{\text{H}_2} = 1.228 \text{ V} - 0.0591(\text{pH}) - 1.481 \text{ V} - 0.0295[\log(\text{pH}_2)] = -0.945 \text{ V} \quad (6)$$

The metal oxide catalysts were created by cathodic electrodeposition of the electrodeposition solution compositions indicated in Table 1 at 250 mA/cm<sup>2</sup> for 30 s unless otherwise noted. Linear voltammetry scans (1 mV/s) on freshly prepared catalysts were preceded by one or more identical scans to polarize and discharge the electrode. Cyclic voltammetry oscillation signals were measured with three cycles from 0.200 to −0.200 V and from 10 to 200 mV/s in 10 mV increments. The capacitance of the catalysts was measured by cyclic voltammetry with three cycles from −0.700 to −1.000 V and from 1 to 200 mV/s. The electrochemical impedance data was collected in 10 mV working potential steps with each step proceeded by a 1.0 min chronocoulometry scan. Impedance was measured from 10<sup>5</sup>–10<sup>−2</sup> Hz with a 10 mV signal amplitude.

X-ray photoelectron spectroscopy (XPS) binding energies were measured both before and after 5 min sputtering with Argon ions (1keV) at 200 nA using a vacuum generator ESCA 2 X-ray photoelectron spectrometer with an Al–Kα source. Powder X-ray crystallography with  $\theta/2\text{-}\theta$  scans at 2°/min were performed on a Siemens D500 Diffraktometer with a Cu source. Oxide samples created on the 20 cm<sup>2</sup> electrodes were scraped off, dried in ambient conditions overnight, disburbed with ethanol, and examined with a Jeol 2011 transmission electron microscopy (TEM) at 200 kV (2.5 pm wavelength) with a lanthanum hexaboride electron source. Scanning electron microscopy/energy dispersive X-ray (SEM/EDX) analysis of the optimized NiFe oxide and the bare platinum support were obtained with a Jeol JSM-5900 scanning electron microscope at 30 KeV. SQUID experiments were conducted using a Quantum Design MPMS XL with a helium-cooled cryostat. Oxide samples created on the 20 cm<sup>2</sup> electrodes were scraped off, dried in ambient conditions overnight, and then encased between two layers of Katon tape and inserted into the center of a clear plastic straw.

## Results

Metal oxide catalysts were formed by cathodic deposition of first row transition metal elements as mixed oxides, singly or in pairs, onto one side of a platinum foil electrode (1 cm<sup>2</sup>). Electrodeposition variables that were explored included the following: buffer composition, buffer concentration, pH, metal ion concentration, metal ion oxidation state, metal salt counter-



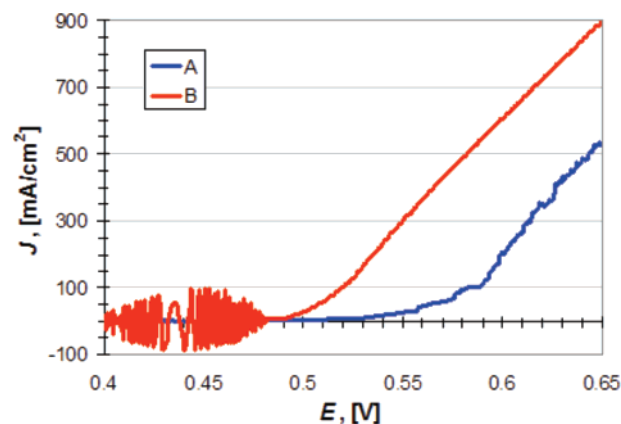
**TABLE 2: Buttlar–Volmer and Resistive Kinetic Data for Oxygen Evolution in 1 M KOH**

oxide	$\alpha_a$	$J_0$ , [A/cm <sup>2</sup> ] $R_{lim}$ , [ohm·cm <sup>2</sup> ]	$J_b$ , [A/cm <sup>2</sup> ]
Mn 0.328	0.841	$4.05 \times 10^{-5}$	0.181
Fe 0.163	0.305	$9.66 \times 10^{-11}$	0.209
Co 0.158	0.660	$1.39 \times 10^{-5}$	0.209
Ni 0.149	0.694	$3.73 \times 10^{-5}$	0.183
Cu 0.309	0.795	$1.12 \times 10^{-6}$	0.581
FeMn 0.205	0.591	$1.19 \times 10^{-7}$	0.187
CoFe 0.130	0.546	$1.16 \times 10^{-5}$	0.149
NiFe <sub>(a)</sub> 0.053	0.008	$9.04 \times 10^{-6}$	0.183
NiCo 0.140	0.515	$2.17 \times 10^{-6}$	0.137
CuFe 0.225	0.535	$3.31 \times 10^{-9}$	0.168
CuNi 0.194	0.778	$1.01 \times 10^{-4}$	0.190

tion, current density, and current duration. All commercially available first row transition metal ion oxidation states were examined. Ratios were explored from 1:10 to 10:1 for electrodeposition solutions containing two different transition metal elements or oxidation states. The list of metal counter anions explored included sulfate, nitrate, phosphate, chloride, perchlorate, and acetate. The majority of experiments focused on electrolytes including ammonium, sodium, and potassium cations and sulfate, sulfite, thiosulfate, persulfate, sulfamate, hydroxide, chloride, perchlorate, (mono/dibasic) phosphate, bicarbonate, carbonate, nitrate, and acetate anions. Organic compounds such as acetic acid, ethanol, methanol, citric acid, acetyl acetate, and ethylenediamine were also examined.

The catalytic kinetic parameters of the metal oxides and pure platinum support were measured with linear voltammetry scans at a potential scan rate of 1 mV/s in 1 M KOH. Exploration of the electrodeposition variables yielded optimized Mn, Fe, Co, Ni, Cu, FeMn, CoFe, NiFe, NiCo, CuFe, and CuNi oxides that demonstrated better catalytic performance than the pure platinum support. The inclusion of Ti, V, Cr, or Zn in the metal oxides did not improve the catalysis of oxygen evolution. The performances of four catalyst compositions are illustrated in Figure 2. The  $\alpha_a$ ,  $J_0$ ,  $R_{lim}$ , and  $J_b$  values for the optimized electrodeposition conditions of the eleven metal compositions are provided in Table 2.

The NiFe oxides demonstrated the best overall catalytic performance for the oxygen evolution reaction because it demonstrates the smallest  $\alpha_a$  values in combination with one of the greatest  $J_0$  values and was therefore selected for further characterization. Similar catalytic parameters were obtained for NiFe oxide catalysts deposited in acidic (pH 2.5) and more basic (pH 5.9) electrodeposition conditions and were identified as NiFe<sub>(a)</sub> and NiFe<sub>(b)</sub>, respectively. The catalytic performance of the NiFe<sub>(a)</sub> conditions were consistently reproducible while the catalysts deposited from NiFe<sub>(b)</sub> required immediate deposition after solution preparation due to iron precipitation at pH 5.9. In the case of each analytical method, the NiFe<sub>(a)</sub> and NiFe<sub>(b)</sub> oxide underwent a 1 mV/s linear voltammetry scan in 1 M KOH after electrodeposition to polarize the catalyst for oxygen evolution and to ensure that the  $\alpha_a$  was less than 0.05. Figure 3 illustrates a Tafel plot of a NiFe<sub>(a)</sub> oxide with an  $\alpha_a$  value of 0.008. An  $\alpha_a$  value of 0.008 represents a >99% ideal electron-transfer efficiency. The pure platinum foil support alone yielded a  $\alpha_a$  of 0.155 from 0.95–1.00 V and a second  $\alpha_a$  of 0.017 from

**Figure 4.** The effect of electrodeposition current density on oxygen evolution catalytic performance by NiFe oxides in 1 M KOH. The NiFe oxides were deposited for 30 s with a current density of  $A = 50$  mA/cm<sup>2</sup>,  $B = 500$  mA/cm<sup>2</sup>.

1.25–1.60 V. Figure 3 illustrates how the four kinetic parameter values ( $\alpha$ ,  $J_0$ ,  $R_{lim}$ , and  $J_b$ ) gave a reasonably complete description of the electrode kinetics at a given overpotential for the oxygen evolution reaction.

The inclusion of extra electrolytes in the electrodeposition solution and the use of significantly greater electrodeposition current densities are two important features in the cathodic electrodeposition method. Cathodic deposition at high-current densities yielded catalysts with improved performance. The effect of electrodeposition current densities on the kinetics of a NiFe oxide created from solutions containing 5.15 Fe(ClO<sub>4</sub>)<sub>2</sub>, 12.85 Ni(ClO<sub>4</sub>)<sub>2</sub>, and 100 mM NH<sub>4</sub>ClO<sub>4</sub> and adjusted to pH 0.5 with H<sub>2</sub>SO<sub>4</sub> is illustrated in Figure 4.

Extra electrolytes in the electrodeposition solution refer to the electrolytes in addition to the metal salts and the acids or bases used to adjust pH. Figure 5 and Table 1 indicate how catalysts with optimal kinetic performance were created from electrodeposition solutions containing ammonium and hard anions. The hardest anions behaved similarly in the majority of conditions although changes in catalytic kinetics were often correlated with the  $pK_a$ 's of the conjugate acids of the anions. Figure 5 illustrates how similar catalytic kinetics resulted when the anions all had only one negative charge due to pH and were at least 1.0 pH unit away from a  $pK_a$  when the electrodeposition solution contained only Fe<sup>2+</sup> ions and had the same ammonium concentration. The electrodeposition conditions of the NiFe oxide catalysts illustrated in Figure 5 are reported in Table 3.

The electrodeposition conditions of NiFe oxide catalysts were explored for optimal hydrogen evolution reaction kinetics. The electrodeposition conditions optimal for oxygen evolution kinetics were empirically determined to also be optimal for hydrogen evolution kinetics. Figure 6 is a Tafel plot of the hydrogen kinetics on a NiFe<sub>(a)</sub> oxide catalyst measured with linear voltammetry scan at a scan rate of −1 mV/s in 1 M KOH. The NiFe<sub>(a)</sub> oxide hydrogen evolution kinetic parameters illustrated in Figure 6 correspond to an  $\alpha_c$  of 0.895, a  $J_0$  of  $-1.85 \times 10^{-6}$  A/cm<sup>2</sup>, a  $R_{lim}$  of 0.293 Ohm·cm<sup>2</sup>, and a  $J_b$  of 0.522 A/cm<sup>2</sup>.

NiFe oxide's oxygen evolution performance was examined by varying the concentration of KOH in the electrolysis solution.

**TABLE 3: The Electrodeposition Solution Conditions for the NiFe Oxides Illustrated in Figure 5**

A	9 mM FeCl <sub>2</sub>	9 mM NiCl <sub>2</sub>	50 mM NH <sub>4</sub> Cl	pH 3.0 w/ HCl
B	9 mM FeSO <sub>4</sub>	9 mM NiSO <sub>4</sub>	25 mM (NH <sub>4</sub> ) <sub>2</sub> SO <sub>4</sub>	pH 3.0 w/ H <sub>2</sub> SO <sub>4</sub>
C	9 mM Fe(ClO <sub>4</sub> ) <sub>2</sub>	9 mM Ni(NO <sub>3</sub> ) <sub>2</sub>	50 mM NH <sub>4</sub> NO <sub>3</sub>	pH 3.0 w/ HNO <sub>3</sub>
D	9 mM Fe(ClO <sub>4</sub> ) <sub>2</sub>	9 mM Ni(ClO <sub>4</sub> ) <sub>2</sub>	50 mM NH <sub>4</sub> ClO <sub>4</sub>	pH 3.0 w/ HNO <sub>3</sub>
E	9 mM FeSO <sub>4</sub>	3 mM Ni <sub>3</sub> (PO <sub>4</sub> ) <sub>2</sub>	50 mM H <sub>2</sub> NH <sub>4</sub> PO <sub>4</sub>	pH 3.0 w/ H <sub>3</sub> PO <sub>4</sub>

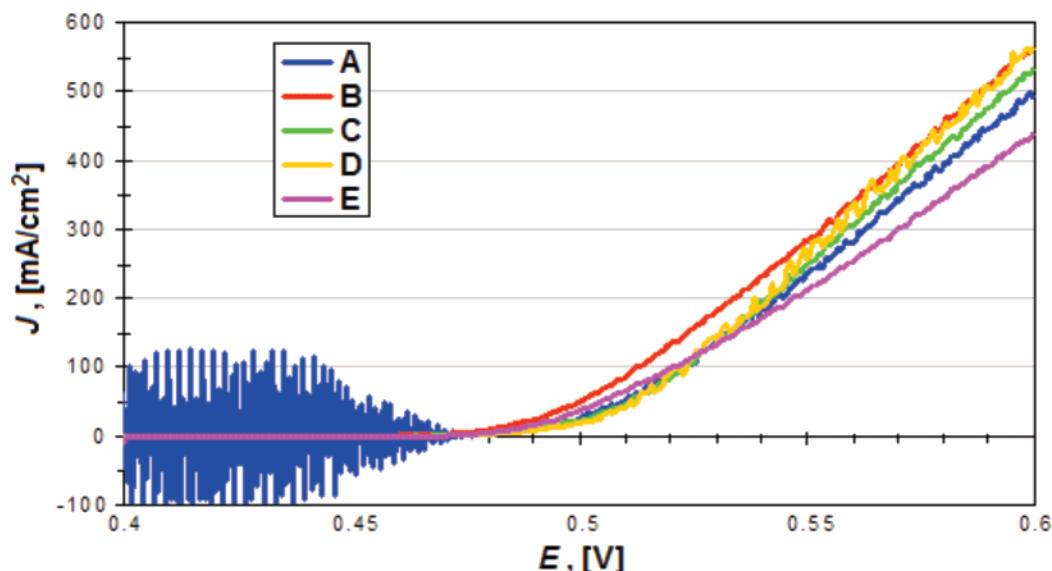


**Figure 5.** The dependence of NiFe oxide oxygen evolution catalytic kinetics upon the composition of hard anions in the electrodeposition solutions reported in Table 3. The catalysts created from compositions A–E were deposited at 250 mA/cm<sup>2</sup> for 30 s and kinetics measured in 1 M KOH.

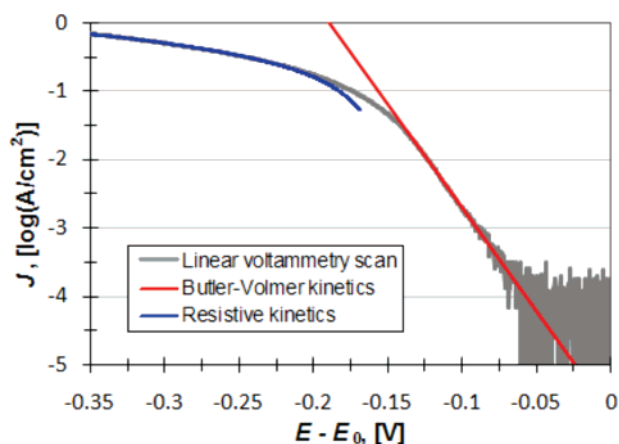


**Figure 6.** A hydrogen evolution Tafel plot for a NiFe<sub>(a)</sub> oxide catalyst prepared from the electrodeposition conditions described in Table 1, and the kinetic data was collected with a linear voltammetry scan at a scan rate of  $-1$  mV/s in 1 M KOH, where  $E_0$  was  $-0.945$  V.

Linear voltammetry scans with a velocity of 1 mV/s were collected on a NiFe oxide in 0.050, 0.100, 0.158, 0.316, 1.00, and 10 000 M KOH electrolytes. The  $\alpha_a$  and  $J_0$  of the NiFe oxide catalyst did not significantly change with respect to KOH concentration. The  $R_{lim}$  remained constant above 0.316 M KOH yet became smaller at lower concentrations of KOH. Figure 7 illustrates the change in  $R_{lim}$  with respect to the KOH concentration by plotting the inverse of  $R_{lim}$  against the log of [KOH]. The dependence of  $R_{lim}$  on the conductivity of the electrolyte was examined by adding KCl to the KOH solution. The presence of chloride ions did not significantly affect oxygen evolution kinetics when  $[OH^-] \geq [Cl^-]$ . The oxygen evolution reaction was severely inhibited when  $[OH^-] < [Cl^-]$ , and the evolution of Cl<sub>2</sub> is dominant as detected by linear voltammetry and olfaction. Other catalyst compositions demonstrated similar pH dependence and reactivity with Cl<sup>-</sup> despite elemental composition.

Cyclic voltammetry and electrochemical impedance spectroscopy were performed on the NiFe oxide oxygen evolution catalyst to identify active half-reactions in the NiFe oxide. Cyclic voltammetry scans of the metal oxide catalysts did not produce peaks that resulted from the net charge transfer of oxidation–reduction couples active within the catalyst. The metal oxide

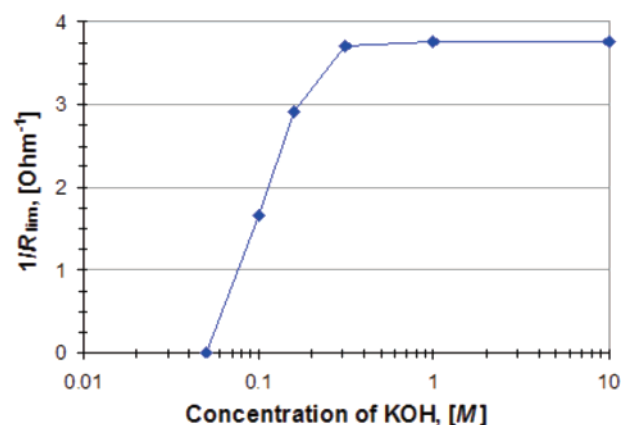


**Figure 7.** Reciprocal of  $R_{lim}$  with respect to the molar concentration of the KOH electrolyte for oxygen evolution on a NiFe<sub>(b)</sub> oxide catalyst.

catalysts developed in this work produced oscillating signals in response to linear changes in working potential and for constant potentials at low-current densities. An oscillating current in response to linear changes in working potential indicates charge movement and rearrangement within the metal oxide rather than net charge transfer between the metal oxide catalyst and the KOH electrolyte. The amplitude and frequency of the oscillation signal of Figure 8 can result in over a coulomb of charge rearrangement within a second for slower scan rates. Analysis of the oscillations revealed that the height of the signals decreased at higher cycle velocities by 1 mA/cm<sup>2</sup> per mV/s for the range of 1–200 mV/s.

The failure of cyclic voltammetry in this system is directly related to the problem of spin conversion in producing the oxygen triplet ground state. Once we attain the triplet ground state in the forward reaction for oxygen evolution, continuation of a cyclic voltammogram would require conversion of triplet dioxygen to some lower spin intermediate in the formation of water. It appears that the entropic (spin conversion) and energetic factors in this process are prohibitive, so the system rearranges charge instead of running cyclically. The paramagnetism of dioxygen insures that there will be a reverse activation energy for production of the first reduction intermediate from dioxygen.

The surface morphology of the NiFe oxide catalyst was electrochemically assessed with cyclic voltammetry where the

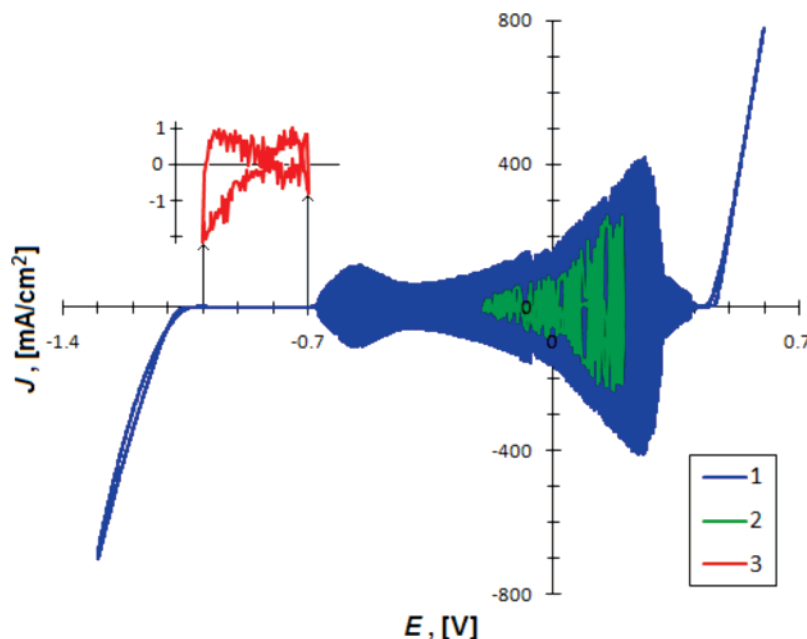


**Figure 8.** Cyclic voltammetry 1 M KOH of a  $\text{NiFe}_{(a)}$  oxide catalyst prepared according to Table 1 at (1) 1 mV/s between 0.600 and  $-1.300$  V, (2) 200 mV/s between 0.200 and  $-0.200$  V, and (3) 200 mV/s between  $-0.700$  and  $-1.000$  V.

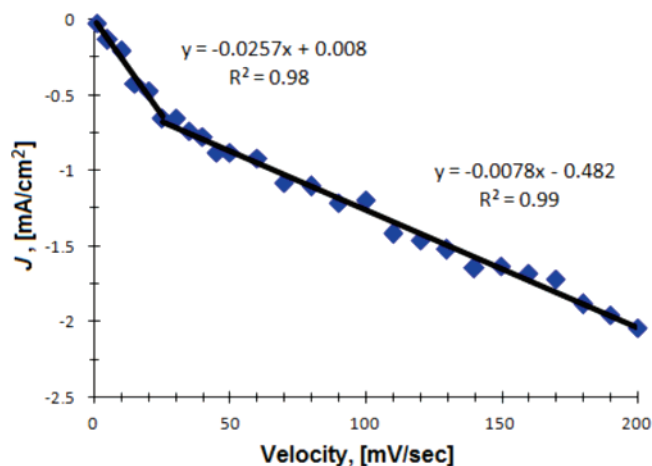


**Figure 9.** The dependence of current density,  $J$ , with respect to cyclic voltammetry velocity on a  $\text{NiFe}_{(a)}$  oxide in 1 M KOH.

catalyst demonstrated the most capacitive behavior (line 3 of Figure 8) according to the procedure of Da Silva et al.<sup>23</sup> The current densities of the negative current peak are plotted against cycle velocity in Figure 9. The reported current densities represent the average current density of the negative peak between  $-0.975$  and  $-1.000$  V due to the noise of the system observed for all cycle velocities. The  $\text{NiFe}$  oxide catalyst demonstrated two regions of linear capacitance characteristic of rugged electrode films.<sup>23</sup> The total differential capacitance,  $C_d$ , was measured to be 25.7 mF, the external differential capacitance,  $C_{d,e}$ , was measured to be 7.8 mF, and the morphology factor,  $\varphi$ , was 0.70.

Chrono potentiometry scans were performed on the  $\text{NiFe}$  oxides to demonstrate that the catalyst was sufficiently stable throughout the period of time required to collect an impedance spectrum. Figure 10 is a chrono potentiometry scan recorded for a  $\text{NiFe}_{(b)}$  oxide catalyst at  $500 \text{ mA/cm}^2$  for 1 h. The short-term stability indicates that the catalyst demonstrates reasonably constant behavior during the time required to collect impedance spectra and is also promising for long-term durability. The  $\text{NiFe}$  oxide catalysts underwent an apparent relaxation through which the catalyst became more efficient with time.

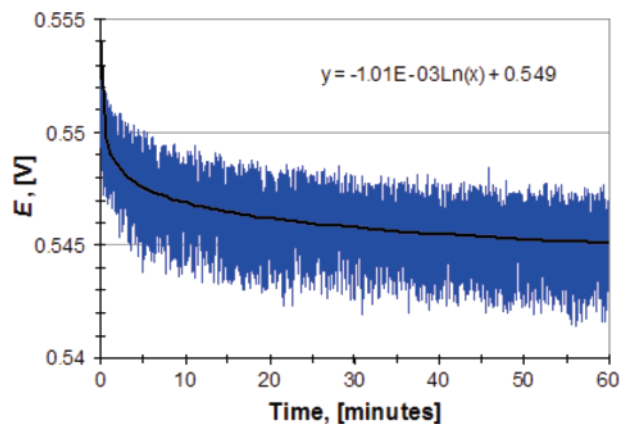


**Figure 10.** A chronopotentiometry scan of a  $\text{NiFe}_{(b)}$  oxide catalyzing oxygen evolution at a current density of  $500 \text{ mA/cm}^2$  for 1 h in 1 M KOH.

Electrochemical impedance spectroscopy (EIS) was measured from  $10^5$  to  $10^{-2}$  Hz utilizing a working potential sine wave with 10 mV amplitude. Impedance spectra were collected on a  $\text{NiFe}$  oxide catalyst from 0.300–0.600 V in 10 mV working potential increments. Each spectrum was preceded with a 2.0 min chrono-coulometry scan to establish a pre-equilibrium after each incremental change in working potential. Nyquist plots of 0.400–0.440 V and 0.450–0.530 V potential ranges are presented in Figure 11, panels A and B, respectively. The spectra did not significantly change above 0.530 V. A novel feature of the Nyquist plots for these catalysts is that the real resistance,  $Z_R$ , of the capacitive loop becomes negative from 0.400 to 0.440 V and  $\sim 3.0$  to 0.5 Hz in the capacitive loop (Figure 11C). A high-frequency inductive loop observed for all working potentials is another novel impedance feature of the metal oxide Nyquist plots (Figure 11C). Only one arc was observed in the inductive loop below 0.390 V. Two arcs were observed above 0.390 V. EIS was performed on the pure platinum support including the insulating backing from 0.900–1.500 V in 50 mV intervals (Figure 11D). The platinum foil only demonstrated the one capacitive loop and then produced noise as the imaginary resistance,  $Z_i$ , approached zero at the lowest frequencies of the capacitive loop. The signal was considered noise when circular

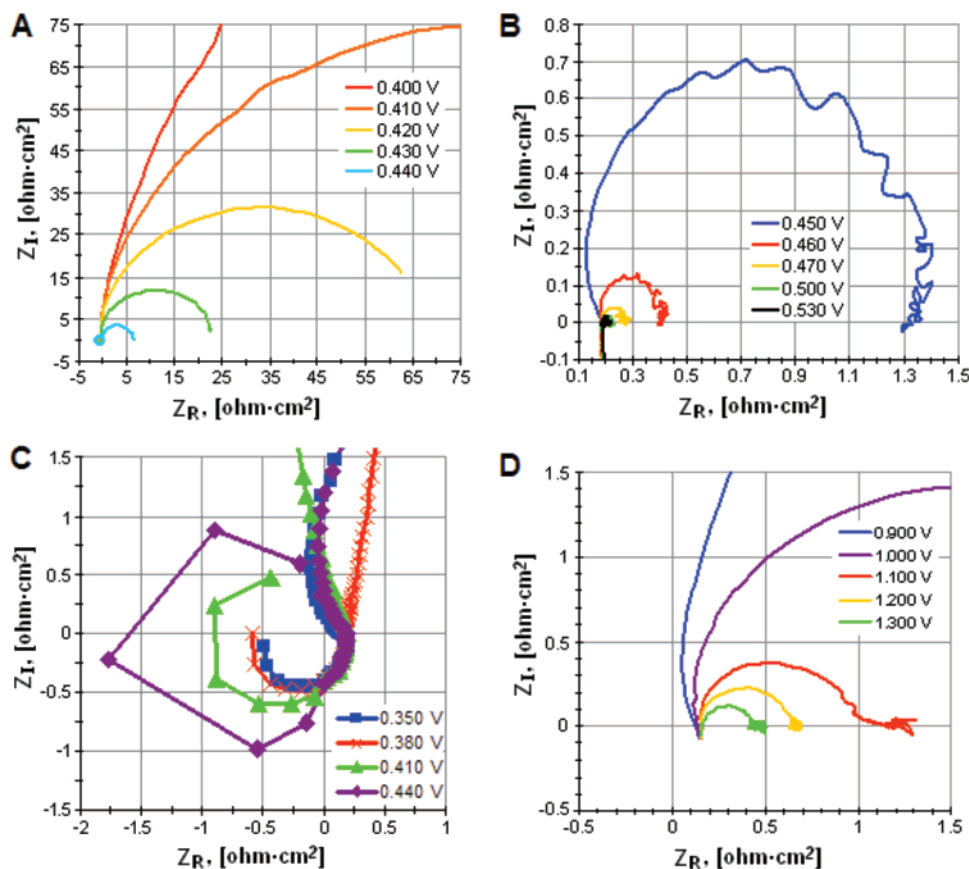


**Figure 11.** EIS Nyquist plots of a NiFe(b) oxide catalyst in 1 M KOH at (A) low working potentials, (B) at medium working potentials, and (C) the inductive loop and negative  $Z_R$  in the capacitive loop. (D) EIS Nyquist plot of the pure platinum control in 1 M KOH.

**TABLE 4: NiFe Oxide Electrodeposition Conditions for XPS and SQUID Analysis**

catalyst	current density (mA/cm <sup>2</sup> )	mM (NH <sub>4</sub> ) <sub>2</sub> SO <sub>4</sub>
A	25	25
B	250 <sup>a</sup>	0
C	250	25

<sup>a</sup> 105 mA/cm<sup>2</sup> for SQUID.

regression of ten consecutive Nyquist plot points yielded correlation values less than 0.50.

XPS was used to determine if higher current densities and an ammonium sulfate electrolyte affected the composition of the NiFe oxide catalyst. The NiFe oxide catalysts were created from solutions containing 9 mM NiSO<sub>4</sub>, 9 mM FeSO<sub>4</sub>, and the electrodeposition current densities and ammonium sulfate concentrations indicated in Table 4. The analysis of the NiFe oxide catalysts with XPS produced the Ni 2p<sup>3/2</sup>, Fe 2p<sup>3/2</sup>, and O 1s multiplets illustrated in Figure 12A–C, respectively. The intensity of the multiplets in Figure 12A–C has been normalized so that the average intensity is 100 000 counts. The XPS multiplets did not change significantly after a 5 min sputtering with 1 KeV argon ions at 200 nA stage. The XPS peaks were broad but did not include any of the metallic states. Both the higher electrodeposition current density (A) and the ammonium sulfate electrolyte (B) shifted the peaks of all three multiplets from binding energies dominated by the hydrated Ni(OH)<sub>2</sub> and FeOOH states to binding energies dominated by the unhydrated NiO and Fe<sub>2</sub>O<sub>3</sub> states (C). The broad multiplet peaks of catalyst C encompass the NiO, Ni<sub>3</sub>O<sub>4</sub>, FeO, Fe<sub>3</sub>O<sub>4</sub>, and the Fe<sub>2</sub>O<sub>3</sub> oxidation states (Ni<sub>3</sub>O<sub>4</sub> binding energies are not available in the NIST database). The peaks of catalyst C are also only 0.1–0.2 eV greater than the binding energies of the NiFe<sub>2</sub>O<sub>3</sub>

oxidation state, which has been indicated with a black line in the Ni 2p<sup>3/2</sup>, Fe 2p<sup>3/2</sup>, and O 1s multiplets.

The optimized NiFe oxide catalyst on the 1 cm<sup>2</sup> platinum support was examined by X-ray powder crystallography both with and without the platinum support. No signals corresponding to nickel or iron could be detected in the noise either with or without the platinum support (Figure 13). Another sample of the optimized NiFe oxide deposited with the 20 cm<sup>2</sup> platinum support was analyzed with TEM and produced diffraction patterns with broad, diffuse rings (Figure 14). Three diffraction patterns contained different sets of the same d-spacings, which include the following: 2.55 (±0.02), 2.44 (±0.04), 2.32 (±0.02), 2.02 (±0.02), 1.51 (±0.02), 1.45 (±0.02), and 1.24 (±0.02) Å. These d-spacings correspond to at least one or more nickel oxide and at least one or more iron oxide, where values for all known anhydrous and hydrous nickel and iron nonmetallic oxidation states were represented two or more times. Diffraction patterns with the same d-spacings were also produced when a second NiFe oxide was prepared from an electrodeposition solution containing the same nickel and iron concentrations and no ammonium sulfate. The deposition current was 25 mA/cm<sup>2</sup>.

TEM images indicated that the optimized NiFe oxide is polycrystalline with crystals ~1 nm and smaller that are well connected with an amorphous phase (Figure 15A). TEM images of the NiFe oxide deposited at 25 mA/cm<sup>2</sup> and without ammonium sulfate indicated crystals sizes up to 5 nm connected with an amorphous phase and that the oxide is prone to fragmenting into loose particles (Figure 15B). SEM images of the NiFe(b) oxide catalyst at 100× and 2000× magnification and the bare platinum support at 2000× magnification are presented in Figure 16A–C, respectively. The elemental analysis averaged from five areas of the catalyst indicated that the NiFe(a)



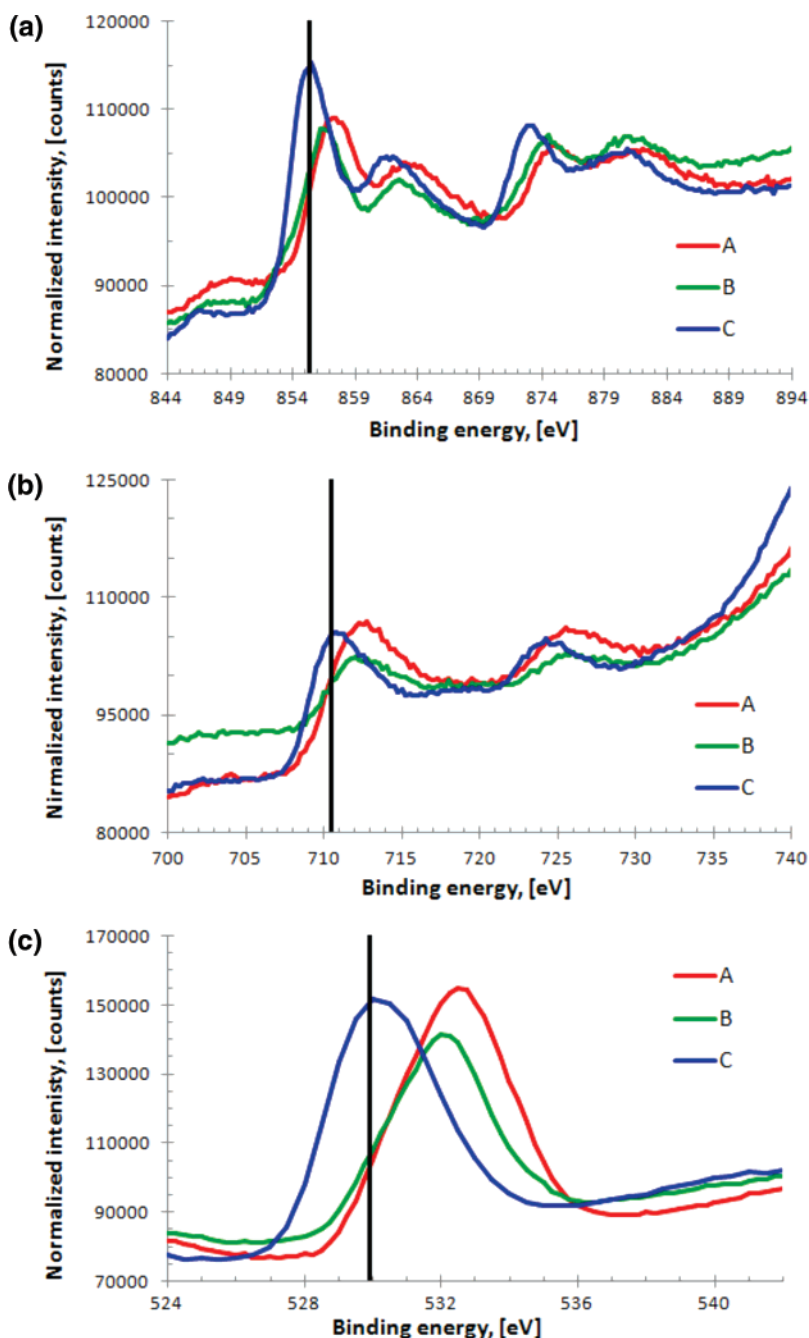


**Figure 12.** (A) XPS Ni 2p<sub>3/2</sub> multiplet of the NiFe oxide catalysts of Table 1. (B) XPS Fe 2p<sub>3/2</sub> multiplet of the NiFe oxide catalysts of Table 1. (C) XPS O 1s multiplet of the NiFe oxide catalysts of Table 1.

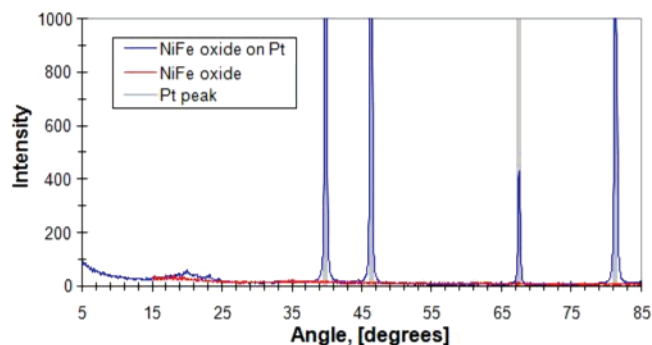


**Figure 13.** X-ray powder crystallography of the NiFe<sub>(a)</sub> oxide with and without the platinum support.

oxide had an atomic ratio of  $68.9 \pm 2.2$  Ni and  $32.2 \pm 1.9\%$  Fe and the NiFe<sub>(b)</sub> oxide had an atomic ratio of  $72.1 \pm 0.4$  Ni

and  $27.8 \pm 0.5\%$  Fe. Potassium did not significantly bind or become impregnated into the NiFe oxide after use in 1 M KOH because it was only detected in one area at 0.17%. Elemental analysis verified that the purity of the platinum (Hauser and Miller) was greater than 99.95% Pt even after repeated catalyst depositions and subsequent cleaning with concentrated sulfuric acid.

NiFe oxide samples prepared according to the electrodeposition conditions indicated in Table 4 were analyzed with a SQUID magnetometer. The sample deposited with ammonium sulfate (C) required 38 V for a current density of 250 mA/cm<sup>2</sup> whereas the sample without ammonium sulfate (B) could only be deposited at 105 mA/cm<sup>2</sup> at 40 V, the maximum voltage of the Agilent power system. Samples A and C were magnetized at 300 K and showed hysteresis loops on SQUID field sweeps. Sample B was paramagnetic (Figure 17). Sample A had the

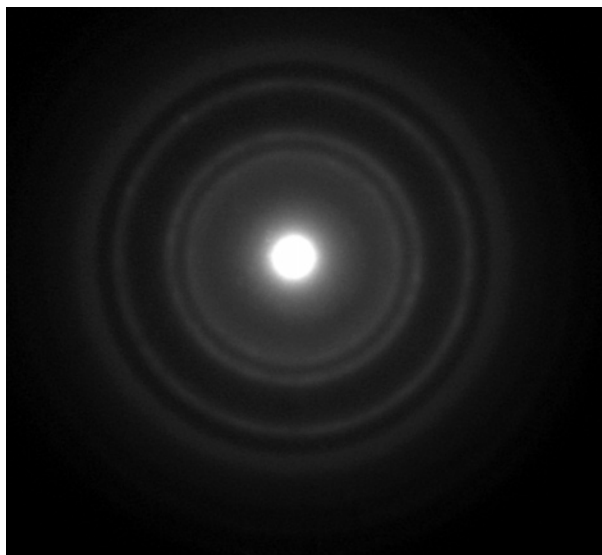


**Figure 14.** TEM diffraction pattern of the optimized NiFe oxide.

largest magnetization (5.79 emu/g); sample C (0.16 emu/g) required the largest coercive force to bring the induced magnetization back to 0 (283 Oe) compared to sample A (113

Oe). Together, the use of a higher current density and an electrolyte containing transition metal nucleophiles (NH<sub>3</sub>) caused the magnetic behavior of the NiFe oxide sample C to be more complex. Figure 18 illustrates a temperature sweep of sample C at 100 G where the sample showed two antiferromagnetic exchange interactions with temperature intercepts of  $-60.5$  K and less than  $-4.5$  K and a paramagnetic exchange interaction with a temperature intercept of  $90.4$  K. Paramagnetic exchange interactions would be consistent with the presence of ferrimagnetic domains in the sample. This behavior reflects the chemical and physical complexity of these catalytic systems.

### Discussion

The systematic optimization of first row transition metal oxide oxygen evolution catalysts was consistent with the assessment of photosystem II and cytochrome C oxidase because the best catalysts were found in the range Mn through Cu on the periodic table of elements. Formation of Fe, Co, and Ni oxides and their combinations gave the greatest overall catalyst performance. Pourbaix<sup>19</sup> shows that these three elements share the following stable solid oxide states: MO, M<sub>3</sub>O<sub>4</sub>, and M<sub>2</sub>O<sub>3</sub>. Mn, which catalyzes oxygen evolution in photosystem II, also forms these stable solid oxide states.<sup>19</sup> The systematic analysis of first-row

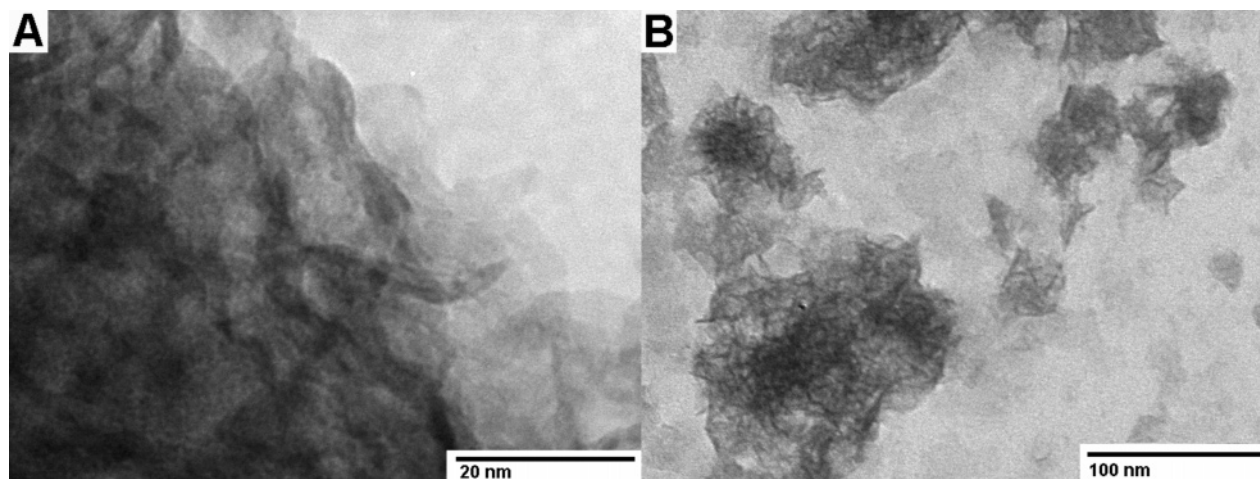


**Figure 15.** TEM images of (A) the optimized NiFe oxide at  $1 \times 10^6$  magnification and (B) the NiFe oxide deposited at  $25 \text{ mA/cm}^2$  and without ammonium sulfate at  $2 \times 10^5$  magnification.

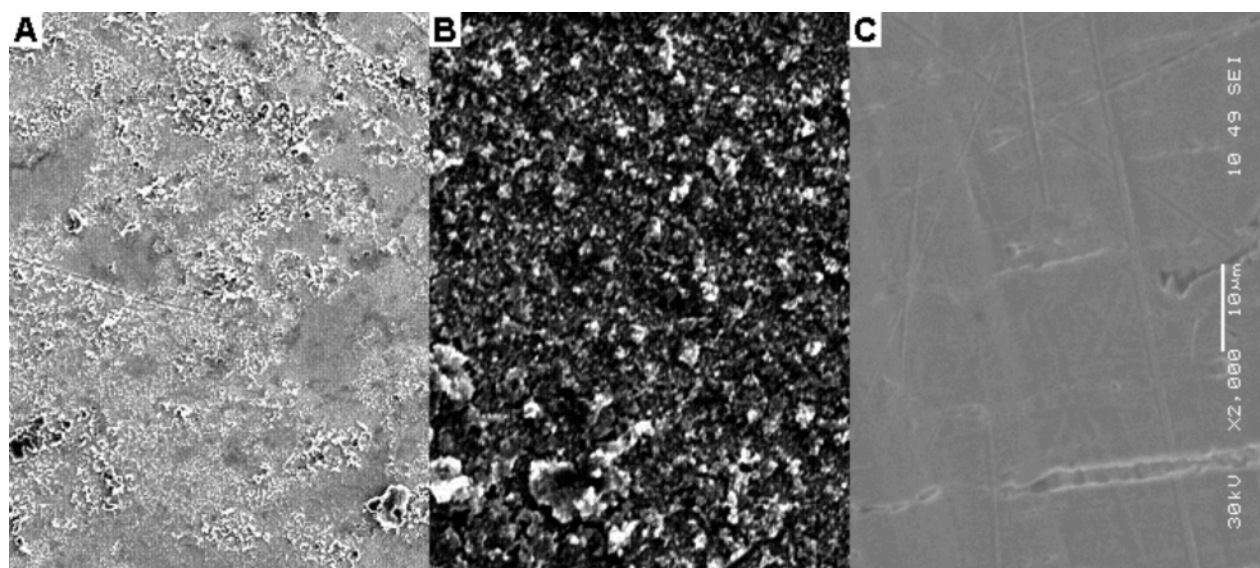


**Figure 16.** SEM images of the NiFe<sub>(b)</sub> oxide catalyst at (A)  $1 \times 10^2$  and (B)  $2 \times 10^3$  magnification and the bare platinum support at (C)  $2 \times 10^3$  magnification.

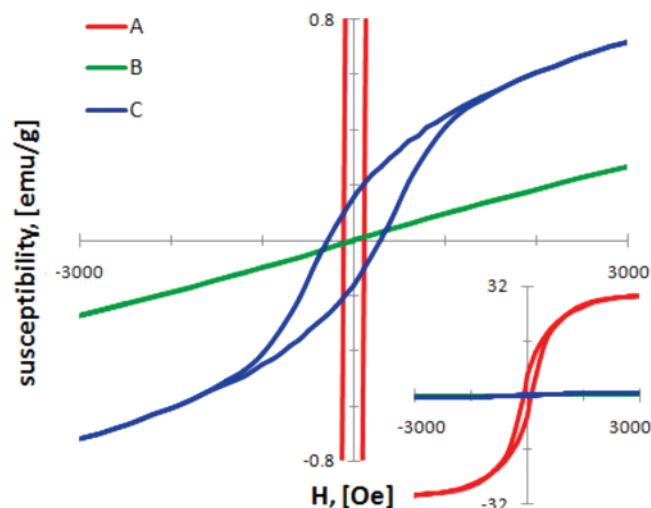


**Figure 17.** SQUID field sweeps of NiFe oxide catalysts prepared according to Table 4 where A was prepared with ammonium sulfate, B was prepared with high-current density, and C was prepared with both ammonium sulfate and high-current density. The inset provides a better perspective of the scale of sample A's magnetization.

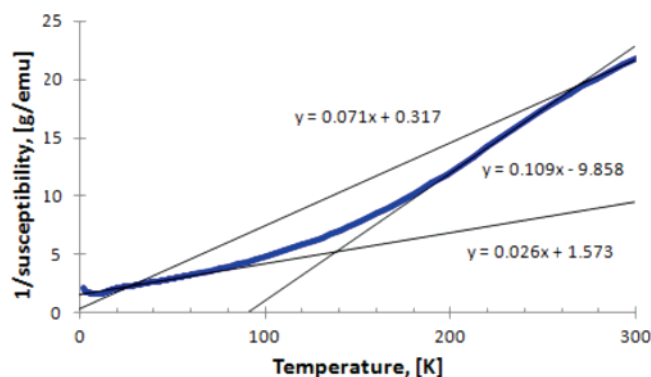


**Figure 18.** SQUID temperature sweep at 100 G for the NiFe oxide sample C of Table 4.

transition metals yielded NiFe oxides that produced the greatest current densities at a given working potential in 1 M KOH. The NiFe oxide was able to achieve the best values for each of the four oxygen evolution kinetic parameters that describe catalyst performance, although each parameter was obtained from different electrodeposition conditions. The hydrogen evolution kinetic parameters demonstrated by the NiFe oxide may mean that the cathodic electrodeposition method may be useful for creating catalysts effective for other reactions of interest.

It is easy to overlook the magnetic properties of materials even though we were specifically concerned about the singlet triplet conversion that is required in the formation of molecular oxygen from water. It has been known for some time that the  $Mn_4$  cluster at the heart of photosystem II exists in an  $S_2$  state.<sup>24a</sup> The  $S_2$  state in photosystem II is magnetically active and is an active participant in the production of the oxygen triplet state. It seems highly likely that effective catalysts for production of oxygen from water or other singlet sources will be magnetically active materials.

The NiFe oxide catalyst in Table 1 had considerably better performance than the NiFe oxides developed by Corrigan et al.,<sup>6–11</sup> which were also created with cathodic electrodeposition. In comparison with the work of Corrigan et al., the two key improvements in the cathodic electrodeposition method developed here are the following: (1) the use of an approximately  $30\times$  greater electrodeposition current densities and (2) the

inclusion of extra nucleophilic electrolytes in the electrodeposition solution, which result in production of catalysts with a magnetization. Both a higher electrodeposition current density and the inclusion of an ammonium sulfate electrolyte in the electrodeposition solution caused the Ni  $2p^{3/2}$ , Fe  $2p^{3/2}$ , and O  $1s$  multiplet peaks to shift from predominantly hydrated nickel and iron oxide binding energies to the predominantly unhydrated binding energies and near the  $NiFe_2O_4$  state.

Analysis of the optimized NiFe oxide with a SQUID magnetometer showed that the magnetic interactions were complex, demonstrating ferro/ferrimagnetic, antiferromagnetic, and paramagnetic behavior at 300 K. The ammonium sulfate buffer caused the ferro/ferrimagnetic behavior at room temperature (Figure 17). This is an expected result because examples of high spin  $Mn^{2+}$ ,  $Fe^{2+}$ ,  $Co^{2+}$ ,  $Ni^{2+}$ , and  $Cu^{2+}$  ions with ammonium or other nucleophilic ligands in aqueous solution are abundant in both inorganic<sup>4</sup> and enzymatic literature.<sup>24b</sup> Theoretical modeling and experiments indicate that the  $CaMn_3O_4$  cluster of photosystem II transitions through high spin states during the catalytic cycle.<sup>1,25</sup> The iron of the heme  $a_3/Cu_B$  catalytic site of cytochrome C oxidase is high spin in the resting state and possibly also in intermediate states.<sup>3,26</sup> Oxygen-activating enzymes commonly have high spin heme iron, non-heme iron, and copper catalytic sites.<sup>27,28</sup> The correlation of ferromagnetic character with approximately ideal electron transfer by the optimized NiFe oxide is evidence that the high spin states in the catalyst facilitated the electron spin inversion required for oxygen evolution.

Corrigan reported a Tafel slope with as little as 17 mV/decade current density<sup>6,7</sup> whereas the  $\alpha_a$  of 0.008 reported in this work corresponds to 14.8 mV/decade current density for the oxygen evolution reaction. While the Tafel slopes were somewhat similar for both catalysts, the smaller  $J_0$  value caused Corrigan's catalyst to operate at  $\sim 200$  mV greater working potentials.<sup>6,7</sup> The significant difference in performance arises because the NiFe oxides  $J_0$  values reported in this work are inferred to be over 4 orders of magnitude greater than the NiFe oxide  $J_0$  values developed by Corrigan et al.<sup>6–11</sup> The  $J_0$  values of Corrigan et al. and most other authors are not reported and the exchange current densities must be inferred from graphical representations. Accurate comparisons of catalytic performances between different work requires the report all four  $\alpha_a$ ,  $J_0$ ,  $R_{lim}$ , and  $J_b$  values.

The deposition of the metal oxides onto the cathode may have been caused by the reduction of protons from  $H_2O$  and  $OH^-$  ligands of the aqueous metal ions rather than hydroxide precipitation produced from the decomposition of hard anion electrolytes as suggested by Corrigan.<sup>10,11</sup> The potentials required for high electrodeposition current densities are well in excess of the reduction potential of hydrogen evolution from water (38 V for 250 mA/cm<sup>2</sup> on the 20 cm<sup>2</sup> electrodes). Electrodeposition at higher current densities would cause the dehydration of the metal oxides observed with XPS by reducing the protons of aqueous ligands to hydrogen gas and leaving oxygen.  $NH_3$  is a stronger base than  $H_2O$ , displacing water ligands on the aqueous metal ions in the electrodeposition solution and would also cause the dehydration of the metal oxides as observed with XPS. NiFe oxides created from electrodeposition solutions containing only  $Cl^-$  anions produced catalytic kinetics similar to other hard anions (Figure 5). The NiFe oxide could not have been formed from hydroxide precipitation through the decomposition of hard anion electrolytes if only  $Cl^-$  was in the electrodeposition solution.

The optimized NiFe oxide is polycrystalline with crystals 1 nm and smaller well connected with amorphous material. The



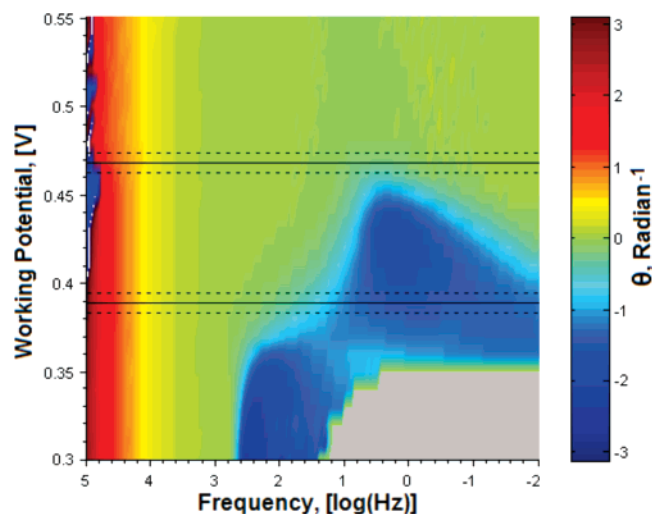


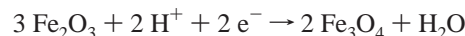
**Figure 19.** The phase angle,  $\theta$ , with respect to both frequency and working potential for a NiFe oxide catalyst in 1 M KOH. The solid lines indicate the electrochemical potential of nickel and/or iron half-reactions while the dashed lines mark the  $\pm 5$  mV boundary of the impedance signal amplitude. The gray area could not be measured due to current disjunction by the electrochemical workstation.

size of the crystals was too small to give a diffraction pattern with X-ray powder crystallography. The d-spacings measured with TEM could correspond to any of the nonmetallic oxidation states. The Ni 2p<sup>3/2</sup>, Fe 2p<sup>3/2</sup>, and O 1s XPS multiplet peaks for the optimized NiFe oxide suggest that the NiFe<sub>2</sub>O<sub>4</sub> oxidation state could be dominant although the peaks were broad enough to encompass all of the other nonmetallic oxidation states available in the NIST database. The dehydration of the NiFe oxide with the use of higher current densities and ammonium electrolytes may have been responsible for increased structural stability and the lack of loose particles observed in Figure 15B. The optimized NiFe oxide has a highly disordered structure. Structural defects are known to correlate with catalytic activity.<sup>16,17</sup>

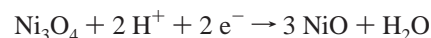
The NiFe catalyst had very mobile charged species in the metal oxide structure. The high frequencies and large amplitudes observed in current density when the working potential was constant or changed with a small velocity (Figure 8) was evidence of highly mobile charged species.<sup>29</sup> Oscillations in current density were spontaneous because the oscillation frequencies observed in Figure 8 correspond to the EIS frequency values (3.0–0.5 Hz) for negative real resistance ( $-Z_R$ ) in the capacitive loop illustrated in Figure 11C. Defects in transition-metal oxides are known to cause electric and ionic conductivity and enable the transport of neutral oxygen atoms through the matrix.<sup>16</sup>

Electrochemical potentials in aqueous solutions are well known so changes in impedance spectra with respect to applied working potentials can be correlated with the redox potentials of known half-reactions. Reduction potentials for stable Ni- and Fe-hydrated oxidation states were calculated for pH 13.84 according to the equations reported in Pourbaix's *Atlas of Electrochemical Equilibria in Aqueous Solutions*<sup>19</sup> because the catalytic sites are expected to be in contact with the aqueous electrolyte. Phase angle,  $\theta$ , changes with respect to working potential (Figure 19) gave the best correlations with impedance spectra. Distinct correlations between the spectra and working potential occurred at  $\sim 0.390$  and  $\sim 0.470$  V for the NiFe oxide catalyst during oxygen evolution. The iron redox reaction of eq 7 correlated with both the phase angle change observed in Figure 19 as well as the appearance of the second arc in the

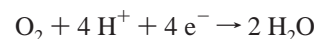
high frequency inductive loop (Figure 11C). The combination of both reactions, 7 and 8, is equal to 0.467 V and correlates with the change in impedance observed at  $\sim 0.470$  V. Reaction 10 is proposed as a basic catalytic mechanism for oxygen evolution by the NiFe oxide.



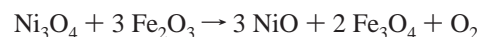
$$E_{(7)} = 1.208 \text{ V} - 0.0591(\text{pH}) = 0.389 \text{ V}_{(7)} \quad (7)$$



$$E_{(8)} = 0.897 \text{ V} - 0.0591(\text{pH}) = 0.078 \text{ V}_{(8)} \quad (8)$$



$$E_{(9)} = 1.228 - 0.0591(\text{pH}) + 0.0147[\log(\text{pO}_2)] = 0.399 \text{ V}_{(9)} \quad (9)$$



$$E_{(10)} = 0.389 \text{ V}_{(7)} + 0.078 \text{ V}_{(8)} - 0.399 \text{ V}_{(9)} = 0.068 \text{ V}_{(10)} \quad (10)$$

All three of the MO, M<sub>3</sub>O<sub>4</sub>, and M<sub>2</sub>O<sub>3</sub> oxidation states observed in eq 10 are only stable for Ni, Co, Fe, and Mn.<sup>19</sup> Empirical optimization of first-row transition metal oxides for catalysis of the oxygen evolution reaction produced the best efficiencies when the catalyst contained Ni, Co, Fe, Mn, or combinations thereof (Table 2), and the implied involvement of these three oxidation states in the catalytic mechanism is consistent with the experimentally demonstrated optimization procedures. The detection of reactions that include the M<sub>3</sub>O<sub>4</sub> oxidation state of Mn, Fe, Co, or Ni is consistent with the literature concerning alkaline oxygen evolution with Ni<sup>30</sup> and NiFe oxide oxygen evolution catalysts<sup>6–11</sup> and other catalysts that included these metals.<sup>31–39</sup> Corrigan et al. presented evidence supporting the involvement of Ni(OH)<sub>2</sub> (hydrated NiO) in NiFe oxide catalytic cycles studied by angle-resolved infrared spectroelectrochemistry,<sup>13</sup> surface-enhanced Raman scattering,<sup>8</sup> and in situ surface Raman spectroscopy<sup>10</sup> as well as FeOOH (hydrated Fe<sub>2</sub>O<sub>3</sub>) by in situ Mössbauer spectroscopy.<sup>9</sup> The NiO<sub>2</sub> oxidation state could correspond to the  $\sim 2.44$  and  $\sim 2.02$  Å d-spacings and was observed with XPS (Figure 12A) in this work and also by Corrigan et al.<sup>10,14,15</sup> although the impedance technique did not indicate that this state actively participated in catalysis.

Small values of inductance have been regularly observed in EIS and were usually dismissed as an experimental artifact resulting from the wiring in the electrochemical cell when the source was not reported as unknown. The high frequency inductive loop of the NiFe oxide catalyst observed here spanned over 3 decades of frequency ( $> 10^5$  to  $\sim 10^2$  Hz). The inductive loop was not observed in the EIS spectra of the platinum without catalyst although a small amount of inductance was observed (Figure 11D) and was therefore not considered an artifact of the experimental setup. High-frequency inductance in combination with negative capacitance and negative resistance has been theoretically explained and modeled by Boukamp to result from multielectron-transfer processes under biased conditions due to multiple species competing for adsorption sites.<sup>40</sup> Experimentally observed high-frequency inductive loops have also been attributed to disordered movement of charge carriers through metal oxide structures by da Silva et al.<sup>41</sup> These explanations may be related to the high frequency inductive loop presented here.



## Summary

We have described the preparation and properties of a series of transition metal oxide electrolysis catalysts for the production of molecular oxygen. The optimum catalyst in this group is a NiFe oxide mixture. When deposited on an inert conductive substrate (in this case Pt foil), this catalyst contained all of the commonly encountered oxides of nickel and iron. The sample did not give an X-ray powder diffraction pattern, but it did possess a magnetization at room temperature. With the use of catalysts of this type and an appropriate hydrogen evolution catalyst, it should be possible in the near future to produce hydrogen and oxygen gas from water at or very near the thermodynamic limit.

**Acknowledgment.** It is a pleasure to acknowledge stimulating discussions with Anjaneyulu Krothapalli and Brenton Greska and support by Florida State University's Sustainable Energy Science and Engineering Center. We are grateful to Eric Lochner and Martech for careful assistance and guidance with the XPS and X-ray experiments, Evan Benbo for SEM and SQUID experiments, and Yan Xin and the NHMFL (NSF Grant DMR-9625692) for TEM experiments. Yan Xin also made seminal observations concerning the magnetic properties of the catalyst.

## References and Notes

- (1) Lundberg, M.; Siegbahn, P. E. M. *Chem. Phys. Lett.* **2005**, *401*, 347–351.
- (2) Pace, R. J.; Ahrling, K. A. *Biochim. Biophys. Acta* **2004**, *1655*, 172–178.
- (3) Schmidt, B.; Hillier, W.; McCracken, J.; Ferguson-Miller, S. *Biochim. Biophys. Acta* **2004**, *1655*, 248–255.
- (4) Figgis, B. N.; Hitchman, M. A. *Ligand Field Theory and Its Applications*; Wiley-VCH: New York, 2000; pp. 92–111, 155–167.
- (5) Halpert, G. J. *J. Power Sources* **1984**, *12* (3–4), 177–192.
- (6) Corrigan, D. A. *J. Electrochem. Soc.* **1987**, *134* (2), 377–384.
- (7) Corrigan's Patent.
- (8) Desilvestro, J.; Corrigan, D. A.; Weaver, M. J. *J. Phys. Chem.* **1986**, *90*, 6408–6411.
- (9) Corrigan, D. A.; Conell, R. S.; Fierro, C. A.; Scherson, D. A. *J. Phys. Chem.* **1987**, *91*, 5009–5011.
- (10) Desilvestro, J.; Corrigan, D. A.; Weaver, M. J. *J. Electrochem. Soc.* **1988**, *135* (4), 885–892.
- (11) Corrigan, D. A.; Bendart, R. M. *J. Electrochem. Soc.* **1989**, *136* (3), 723–728.
- (12) Bendert, R. M.; Corrigan, D. A. *J. Electrochem. Soc.* **1989**, *136* (5), 1369–1374.
- (13) Nazri, G.; Corrigan, D. A.; Maheswari, S. P. *Langmuir* **1989**, *5*, 17–22.
- (14) Corrigan, D. A.; Knight, S. J. *Electrochem. Soc.* **1989**, *136* (3), 613–619.
- (15) Carpenter, M. K.; Corrigan, D. A. *J. Electrochem. Soc.* **1989**, *136* (4), 1022–1026.
- (16) Lankhorst, M. H. R.; Bouwmeester, H. J. M.; Verweij, H. J. *Am. Chem. Soc.* **1997**, *80* (9), 2175–98.
- (17) Merkle, R.; Maier, J. **2006**, *38*, 141–145.
- (18) Rodil, E.; Persson, K.; Vera, J. H.; Wilczek-Vera, G. *AIChE J.* **2001**, *47* (12), 2807–2818.
- (19) Pourbaix, M. *Atlas of Electrochemical Equilibria in Aqueous Solution*; Cebalcor: Brussels, 1974.
- (20) Broeker, W. S. *How to Build a Habitable Planet*; Eldigo Press: New York, 2002.
- (21) Onda, K.; Kyakuno, T.; Hattori, K.; Ito, K. *J. Power Sources* **2004**, *132*, 64–70.
- (22) Roy, A.; Watson, S.; Infield, D. *Int. J. Hydrogen Energy* **2006**, *31*, 1964–1979.
- (23) Da Silva, L. M.; De Faria, L. A.; Boodts, J. F. C. *Electrochim. Acta* **2001**, *47*, 395–403.
- (24) (a) Koulouglitis, D.; Schweitzer, R. H.; Brudvig, G. W. *Biochemistry* **1997**, *36*, 9735. (b) Nelson, D. L.; Cox, M. M. *Lehninger Principles of Biochemistry*; Worth Publishers: New York, 2000.
- (25) Isobe, H.; Shoji, M.; Koizumi, K.; Kitagawa, Y.; Yamanaka, S.; Kuramitsu, S.; Yamaguchi, K. *Polyhedron* **2005**, *24*, 2767–2777.
- (26) Han, S.; Takahashi, S.; Rousseau, D. L. *J. Biol. Chem.* **2000**, *275* (3), 1910–1919.
- (27) Decker, A.; Solomon, E. I. *Curr. Opin. Chem. Biol.* **2005**, *9*, 152–63.
- (28) Holm, R. H.; Kennepohl, P.; Solomon, E. I. *Chem. Rev.* **1996**, *96*, 2239–2314.
- (29) de Paula, J.; Atkins, P. *Physical Chemistry*, 7th Edition; W. H. Freeman: New York, 2001.
- (30) Arulraj, I.; Trivedi, D. C. *J. Hydrogen Energy* **1989**, *14* (12), 893–898.
- (31) Singh, R. N.; Singh, N. K.; Singh, J. P. *Electrochim. Acta* **2002**, *47*, 3873–3879.
- (32) Godinho, M. I.; Catarino, M. A.; da Silva Pereira, M. I.; Mendonca, M. H.; Costa, F. M. *Electrochim. Acta* **2002**, *47*, 4307–4314.
- (33) Elizalde, M. P.; Gonzalez, M.; Garcia, E.; Davila, M. M.; Poillat, G. *J. Electrochem. Soc.* **1997**, *144* (9), 263–266.
- (34) Ponce, J.; Rehspringer, J. -L.; Poillat, G.; Gautier, J. L. *Electrochim. Acta* **2001**, *46*, 3373–3380.
- (35) Rashkova, V.; Kitova, S.; Konstantinov, I.; Vitanov, T. *Electrochim. Acta* **2002**, *47*, 1555–1560.
- (36) Ponce, J.; Rios, E.; Rehspringer, J. -L.; Poillat, G.; Chartier, P.; Gautier, J. L. *J. Solid State Chem.* **1999**, *145*, 23–32.
- (37) Cattarin, S.; Guerriero, P.; Musiani, M. *Electrochim. Acta* **2001**, *46*, 4229–4234.
- (38) Rios, E.; Chen, Y. Y.; Gracia, M.; Marco, J. F.; Gancedo, J. R.; Gautier, J. L. *Electrochim. Acta* **2001**, *47*, 559–566.
- (39) Prakash, J.; Tryk, D. A.; Yeager, E. B. *J. Electrochem. Soc.* **1999**, *146* (11), 4145–4151.
- (40) Boukamp, B. *Solid State Ionics* **2001**, *143*, 47–55.
- (41) da Silva, L. M.; de Faria, L. A.; Boodts, J. F. C. *J. Electroanal. Chem.* **2002**, *532*, 141–150.